PAPER • OPEN ACCESS

Distinguishing the XUV-induced Coulomb explosion dynamics of iodobenzene using covariance analysis

To cite this article: Tiffany Walmsley *et al* 2024 *J. Phys. B: At. Mol. Opt. Phys.* **57** 235101

View the article online for updates and enhancements.

Distinguishing the XUV-induced Coulomb explosion dynamics of iodobenzene using covariance analysis

Tiffany Walmsley[1] ⓘ, **Felix Allum**[2,3] ⓘ, **James R Harries**[4], **Yoshiaki Kumagai**[5] ⓘ, **Suzanne Lim**[1], **Joseph McManus**[1], **Kiyonobu Nagaya**[6], **Mathew Britton**[2,3], **Mark Brouard**[1] ⓘ, **Philip Bucksbaum**[3], **Mizuho Fushitani**[7] ⓘ, **Ian Gabalski**[3,8] ⓘ, **Tatsuo Gejo**[9] ⓘ, **Paul Hockett**[10] ⓘ, **Andrew J Howard**[3,8] ⓘ, **Hiroshi Iwayama**[11] ⓘ, **Edwin Kukk**[12], **Chow-shing Lam**[1] ⓘ, **Russell S Minns**[13] ⓘ, **Akinobu Niozu**[14] ⓘ, **Sekito Nishimuro**[15] ⓘ, **Johannes Niskanen**[12], **Shigeki Owada**[16,17] ⓘ, **Weronika O Razmus**[13], **Daniel Rolles**[18] ⓘ, **James Somper**[1] ⓘ, **Kiyoshi Ueda**[19], **James Unwin**[1], **Shin-ichi Wada**[20], **Joanne L Woodhouse**[13], **Ruaridh Forbes**[2] ⓘ, **Michael Burt**[1,*] ⓘ **and Emily M Warne**[1,*] ⓘ

[1] Chemistry Research Laboratory, Department of Chemistry, University of Oxford, Oxford OX1 3TA, United Kingdom

[2] Linac Coherent Light Source, SLAC National Accelerator Laboratory, 2575 Sand Hill Road, Menlo Park, CA 94025, United States of America

[3] PULSE Institute, SLAC National Accelerator Laboratory, 2575 Sand Hill Road, Menlo Park, CA 94025, United States of America

[4] National Institutes for Quantum Science and Technology (QST), SPring-8, 1-1-1 Kouto, Sayo, Hyogo 679-5148, Japan

[5] Department of Applied Physics, Tokyo University of Agriculture and Technology, Tokyo, Japan

[6] Department of Physics, Kyoto University, Kyoto 606-8502, Japan

[7] Department of Chemistry, Graduate School of Science, Nagoya University, Nagoya, Aichi 464-8602, Japan

[8] Department of Applied Physics, Stanford University, Stanford, CA 94305-4090, United States of America

[9] Graduate School of Material Science, University of Hyogo, Kouto 3-2-1, Kamigori-cho, Ako-gun, Hyogo 678-1297, Japan

[10] National Research Council of Canada, 100 Sussex Dr., Ottawa ON K1A 0R6, Canada

[11] Institute for Molecular Science, Okazaki 444-8585, Japan

[12] Department of Physics and Astronomy, University of Turku, FI-20014 Turku, Finland

[13] School of Chemistry, University of Southampton, Highfield, Southampton SO17 1BJ, United Kingdom

[14] Graduate School of Humanities and Social Sciences, Hiroshima University, Higashi-Hiroshima 739-8524, Japan

[15] Department of Chemistry, School of Science, Tokyo Institute of Technology, 2-12-1 W4-10 Ookayama, Meguro-ku, Tokyo 152-8551, Japan

[16] Japan Synchrotron Radiation Research Institute, Kouto 1-1-1 Sayo, Hyogo, Japan

[17] RIKEN SPring-8 Center, Kouto 1-1-1 Sayo, Hyogo, Japan

[18] J. R. Macdonald Laboratory, Department of Physics, Kansas State University, Manhattan, KS 66506, United States of America

[19] Department of Chemistry, Tohoku University, Sendai 980-8578, Japan

[20] Graduate School of Advanced Science and Engineering, Hiroshima University, Higashi-Hiroshima 739-8526, Japan

* Authors to whom any correspondence should be addressed.

CrossMark

Abstract

The primary and secondary fragmentation dynamics of iodobenzene following its ionization at 120 eV were determined using three-dimensional velocity map imaging and covariance analysis. Site-selective iodine 4d ionization was used to populate a range of excited polycationic parent states, which primarily broke apart at the carbon-iodine bond to produce I^+ with phenyl or phenyl-like cations ($C_nH_x^+$ or $C_nH_x^{2+}$, with $n = 1-6$ and $x = 1-5$). The molecular products were produced with varying degrees of internal excitation and dehydrogenation, leading to stable and unstable outcomes. This further allowed the secondary dynamics of $C_6H_x^{2+}$ intermediates to be distinguished using native-frame covariance analysis, which isolated these processes in their own centre-of-mass reference frames. The mass resolution of the imaging mass spectrometer used for these measurements enabled the primary and secondary reaction channels to be specified at the level of individual hydrogen atoms, demonstrating the ability of covariance analysis to comprehensively measure the competing fragmentation channels of aryl cations, including those involving intermediate steps.

Supplementary material for this article is available online

1. Introduction

Aryl polycations are versatile reactive intermediates that play essential roles in aryl-carbon bond formation as well as the photodegradation of pesticides and antibiotics [1–4]. Even the simplest aryl group, phenyl, can lead to wide-ranging outcomes depending on the charge distribution of the ionic state being accessed. Excited phenyl polycations can undergo electronic relaxation within a few hundred femtoseconds to populate a broad range of states with varying degrees of vibrational activity, leading to geometries that are significantly distorted relative to the highly symmetric neutral ground state [5–12]. For example, the most stable isomers of the phenyl monocation and dication include linear ring-opened configurations in addition to structures that resemble neutral phenyl. Moreover, as the internal energy of a phenyl polycation increases, fragmentation can also occur through hydrogen loss or dissociation into smaller hydrocarbon moieties. These processes are facilitated by hydrogen transfer or skeletal rearrangements and usually favor the formation of dissociated products such as acetylene [5, 8, 10, 12, 13].

Given that aryl groups are key building blocks of larger aromatic molecules, disentangling their competing fragmentation dynamics will help elucidate the behavior of a wide range of reactions. For example, the formation and stability of phenyl polycations are closely connected to the excited-state fragmentation dynamics of polyaromatic hydrocarbons (PAHs), which make up approximately 10%–20% of the carbon in the Milky Way [14, 15]. When PAHs are ionized to highly-excited states by extreme ultraviolet (XUV) light, they undergo structural distortions, isomerization, bond cleavage, and ultimately fragmentation through hydrogen or acetylene loss [13, 16–25]. These fragmentation mechanisms are similar to those observed for phenyl polycations under the same conditions and have heavily contributed to our understanding of the evolutionary chemistry of the interstellar medium [13, 15, 26–28].

In this report, three-dimensional velocity map imaging (VMI) mass spectrometry is used to disentangle the fragmentation dynamics of phenyl polycations produced following the XUV-induced ionization of iodobenzene [29–31]. Dissociative ionization of iodobenzene has previously been shown to produce neutral iodine and $C_6H_5^+$, where the latter can further fragment into smaller carbon-containing products [32–34]. Molecular Coulomb explosion experiments on iodobenzene have additionally produced I^+ with $C_6H_5^+$ or $C_6H_5^{2+}$ [35]. Here, the secondary fragmentation dynamics of these phenyl cations are examined in greater detail. Polycationic parent molecules were created using ultrashort and intense 120 eV pulses, which provide sufficient energy to surpass the iodine 4d ionization threshold and yield highly-charged species. The parent ions produced by this method are unstable and, following charge rearrangement, Coulomb explode into ionic or neutral products with momenta that are defined by the contributing fragmentation mechanisms [36–41]. These fragmentation pathways were differentiated by measuring and correlating the relative fragment momenta using recoil-frame covariance analysis [42–47]. In this case,

the mass resolution of the employed VMI spectrometer further allowed the fragment ions to be assigned with 1 Da precision, which enabled fragmentation reactions involving various C_nH_x species ($n = 1-6$ and $x = 1-5$) to be investigated [48].

In these experiments, the recoil-frame covariance approach is applied using the Newton-frame representation, with the three-dimensional ion momentum information from the VMI spectrometer as input [45]. This enables averaged relative fragment momenta to be imaged within the reference frame of the primary Coulomb explosion, or within the 'native' frame of an intermediate [49], as has been demonstrated for the XUV-induced fragmentation of 1- and 2-iodopropane polycations under similar conditions to the measurements reported here [40, 50]. In the current work, these covariance methods are used to map the fragmentation dynamics of mono- or dicationic phenyl fragments produced following primary Coulomb explosions that break the carbon-iodine bond of iodobenzene, both in the primary reference frame of the initial Coulomb explosion and the native frame of the dicationic phenyl intermediate. In doing so, we demonstrate the ability of these techniques to visualize complex and competing fragmentation dynamics involving fragments that differ in mass by as little as 1 Da, and illustrate the potential of extending these experimental and analytical methods to study the fragmentation dynamics of complex molecules with relatively long-lived excited states.

2. Methods

2.1. Experimental

Iodobenzene fragment momenta were recorded at the soft x-ray beamline (BL1) of the SPring-8 Angstrom Compact free electron LAser (SACLA), using the VMI spectrometer of Ueda and coworkers [29, 30, 40, 48, 51]. A pulsed molecular beam of iodobenzene was expanded into the laser interaction region of the spectrometer and crossed at 45° by 120 eV (10.3 nm) pulses from SACLA, which lie above the iodine 4d ionization threshold in energy and facilitate multiple ionization of the parent molecule through inner-shell photoionization and subsequent Auger–Meitner decay [52]. The absorption cross-sections of iodine, carbon, and hydrogen at 120 eV are approximately 1.4 Mb, 0.1 Mb, and 0.01 Mb, respectively, which created preferential conditions for site-selective ionization of the iodine atom [53, 54]. The XUV pulses were produced at 60 Hz with a bandwidth of 2% and a pulse duration of 30 fs [55]. The average XUV pulse energy was determined to be $11.4 \pm 1.1\,\mu$J, using shot-to-shot measurements made by a gas intensity monitor (figure S1 of the supplementary material). This was reduced to $1.33 \pm 0.13\,\mu$J in the spectrometer due to the combined transmission of the beamline (90%) and a $0.65\,\mu$m zirconium filter (13%) [55, 56]. A Kirkpatrick–Baez mirror system was used to focus the XUV pulses to about $10\,\mu$m ($1/e^2$) in the laser interaction region, yielding a Gaussian intensity of 1.1×10^{14} W cm^{-2}.

Ions generated by the XUV pulses were accelerated by the VMI potentials through a field-free region of the spectrometer

and onto a dual micro-channel plate array coupled to a hexanode delay-line detector [48]. Approximately eight ions were detected per laser shot on average. The ion momenta ($\vec{p}$) and mass-to-charge (m/z) ratios were then determined using the spatial coordinates (x, y) of the detector, yielding $\vec{p_x}$ and $\vec{p_y}$, and the ion times-of-flight (t). The arrival times were precisely measured relative to the electronic trigger of the XUV beam, which allowed the momentum distribution along the time-of-flight axis ($\vec{p_z}$) to be recovered for each ion hit, and hence for the three-dimensional momentum information to be determined. The overall momentum resolution of these measurements was assumed to be eight atomic units (a.u., defined as $\hbar/a_0$, where 1 a.u. = 1.993×10^{-24} kg m s^{-1}). This was based on previous iodopropane data from SACLA BL1 recorded under identical VMI conditions, where covariance analysis was used to determine the Gaussian standard deviation inherent in the summed momenta of a correlated ion pair, which should otherwise equal zero due to conservation of momentum [50].

2.2. Covariance analysis

With the three-dimensional ion momenta as input, covariance imaging methods were used to determine the relative momenta of sets of correlated ions produced through the same fragmentation channels [40, 45]. This was accomplished by two- and three-fold covariance methods, which obtain the relative momentum distributions of ion pairs or trios, respectively [43–47, 57, 58]. Relative ion momenta are displayed here in a Newton-frame representation, with the momenta of the ions of interest shown relative to the trajectory of a reference ion. For two-fold covariance, the momentum of the remaining mass of the molecule (if any) is inferred through conservation of momentum. It should be noted that, for covariance between sets of ions where one or more hydrogen atom is unaccounted for (e.g. $I^+ + C_6H_4{}^+$), the charge states of any missing hydrogens cannot be assigned; neutral hydrogen atoms were not measurable, and any H$^+$ fragments produced were too energetic to be effectively focused onto the detector under the applied VMI conditions. Therefore, no meaningful covariances were observed with any protons.

By applying momentum constraints to the ions used in the covariance calculations, different fragmentation processes involving the same sets of product ions were distinguished and separately analyzed. This approach has been applied to detail the polycation fragmentation dynamics of 1- and 2-iodopropane [40, 50], and, as will be detailed later, is used here to differentiate the production of C_nH_x ($n = 1-6$ and $x = 1-5$) mono- or dications following the Coulomb explosion of iodobenzene. The subsequent breakup mechanisms of short-lived phenyl or C_nH_x intermediates were also analyzed independently of the primary Coulomb explosion channels by performing covariance calculations within the native frame of the intermediate [40, 49, 50]. Secondary products contain momentum contributions from both the primary Coulomb explosion and the secondary dissociation process, and removing the contribution to

the hydrocarbon fragment from the former (which is encoded here in the momentum of the primary I^+ product) allows the energetics of the secondary process to be analyzed in isolation.

To account for any shot-to-shot fluctuations in the experiment that introduced false correlations into the covariance output, such as in the pulse energy, a contingent covariance correction was employed [59]. This method sorts and splits the ion data according to their associated pulse energies, with each bin containing an equal number of laser shots [40, 60–62]. Here, ten bins were used (see section 1 of the supplementary material). Covariance was calculated for each bin and averaged over all bins. By integrating over the resulting positive covariance, intensities corresponding to the relative yields of different fragmentation channels were obtained. The corresponding uncertainties associated with these intensities were extracted using an adapted bootstrapping method, where covariance was calculated for 100 data subsets, each made up of 50 000 laser shots (out of 920 490 total laser shots). This resulted in approximately Gaussian distributions of integrated intensities, from which standard deviations were obtained. An example of this process is provided in figure S2 of the supplementary material.

3. Results and discussion

The mass spectrum in figure 1(a) illustrates the iodobenzene fragment ions detected following single (and multi-) photon XUV ionization at 120 eV. These include I^{1-6+} as well as $C_nH_x^+$ (with n ranging from $1-6$ and x from $1-5$). The extensive ionization of the iodine fragments is a consequence of the site-selective nature of the XUV probe pulse, as discussed previously. To determine which ions were generated as cofragments, time-of-flight covariance analysis was first used to determine the relative degrees of ion-ion correlation [42, 59]. The result is shown in figure 1(b), where the off-diagonal elements correspond to ion pairs that are statistically produced from the same fragmentation channel (or channels). The diagonal elements represent the autocovariances. Many correlated ion pairs are distinguishable and, assuming a uniform detection efficiency for all ionic fragments, the observed covariance intensities can be used as a proxy for their relative populations and hence their contributions to the overall mass spectrum [59]. This assumption should be valid over at least small m/z ranges, as the ions will impact the detector with similar kinetic energies along the time-of-flight axis.

The most prominent covariances in figure 1(b) are between I^+ and several of the $C_nH_x^+$ fragments, indicating preferential cleavage of the C–I bond. Covariances involving I^{2-6+} as cofragments are essentially negligible in comparison. In this analysis, fragments differing in mass by a single hydrogen atom are distinguishable due to the temporal resolution of the delay-line detector. This is highlighted by the black box in figure 1(b), which is magnified in figure 1(c)

to illustrate the well-defined $C_nH_x^+$ ($n = 3-6$, $x = 1-5$) features. Correlations can also be seen between pairs of carbon-containing cations ($C_nH_x^+ + C_{6-n}H_y^+$, where $x + y \leqslant 5$), particularly when $n = 2$ or 3. Weak correlations indicating two-body recoil additionally exist between $C_nH_x^+$ and $C_{6-n}H_yI^+$ pairs but are about 100 times less intense than the $C_nH_x^+$ and I^+ covariances. This indicates that only a relatively small amount of iodobenzene polycations break apart via primary C–C bond cleavage; hence, these features are not considered further here.

The exact mechanisms giving rise to each correlated ion pair cannot be fully determined from the time-of-flight data in figure 1(b). However, the gradients of the linear covariant time-of-flight features, which are reported in table S1 of the supplementary material, can be used to infer whether the co-ions involved originate from two- or many-body fragmentation mechanisms [63]. For example, pairs of ions generated in a two-body Coulomb explosion, such as I^+ and $C_6H_5^+$, recoil with equal and opposite momenta. Their times-of-flight, which correspond to the components of the fragment momenta directed along the time-of-flight axis ($\vec{p}_z$), should therefore exhibit perfect inverse correlation and produce a gradient of -1 in the time-of-flight covariance output.

Features arising from many-body fragmentation processes are generally more diffuse in figure 1(b), as the fragment momenta are not restricted to recoil along a line as in the two-body case. Their gradients can therefore deviate from -1 and have correlation coefficients closer to zero. For example, the covariances between I^+ and the $C_nH_x^+$ fragments where $n < 6$ must, at minimum, originate from three-body processes, which can in principle produce three cations, or two cations with a neutral fragment. The gradients observed in figure 1(c) for the $C_nH_x^+$ fragments spanning $C_3H_2^+$ to $C_6H_2^+$ range from -0.46 to -0.91. These are virtually identical to the $-m(C_nH_x^+)/m(C_6H_5^+)$ ratios for these ions, which cover -0.49 to -0.96, respectively. This indicates that these mechanisms proceed through an initial charge separation via primary Coulomb explosion into I^+ and $C_6H_5^+$ (ignoring any H/H$^+$ loss), which is followed by a secondary breakup of the carbon-containing intermediate fragment into a cation and one or more neutral moieties [63, 64]. Assuming that any momentum gained in the secondary dissociation step is negligible compared to the fraction of momentum obtained from the intermediate (for example, due to only one of the secondary fragments being charged), the momenta of the I^+ and secondary product ions can be expressed as follows, where $\vec{p}(I^+) = -\vec{p}(C_6H_5^+)$:

$$\frac{p\left(C_nH_x^+\right)}{p\left(I^+\right)} \approx \frac{m\left(C_nH_x^+\right)}{m\left(C_6H_5^+\right)}. \tag{1}$$

Put another way, if a secondary dissociation produces two products with relatively little kinetic energy release, as would be expected here for the breakup of a singly-charged intermediate after it has moved far enough away from the I^+ to avoid significant Coulombic repulsion, then the momenta of
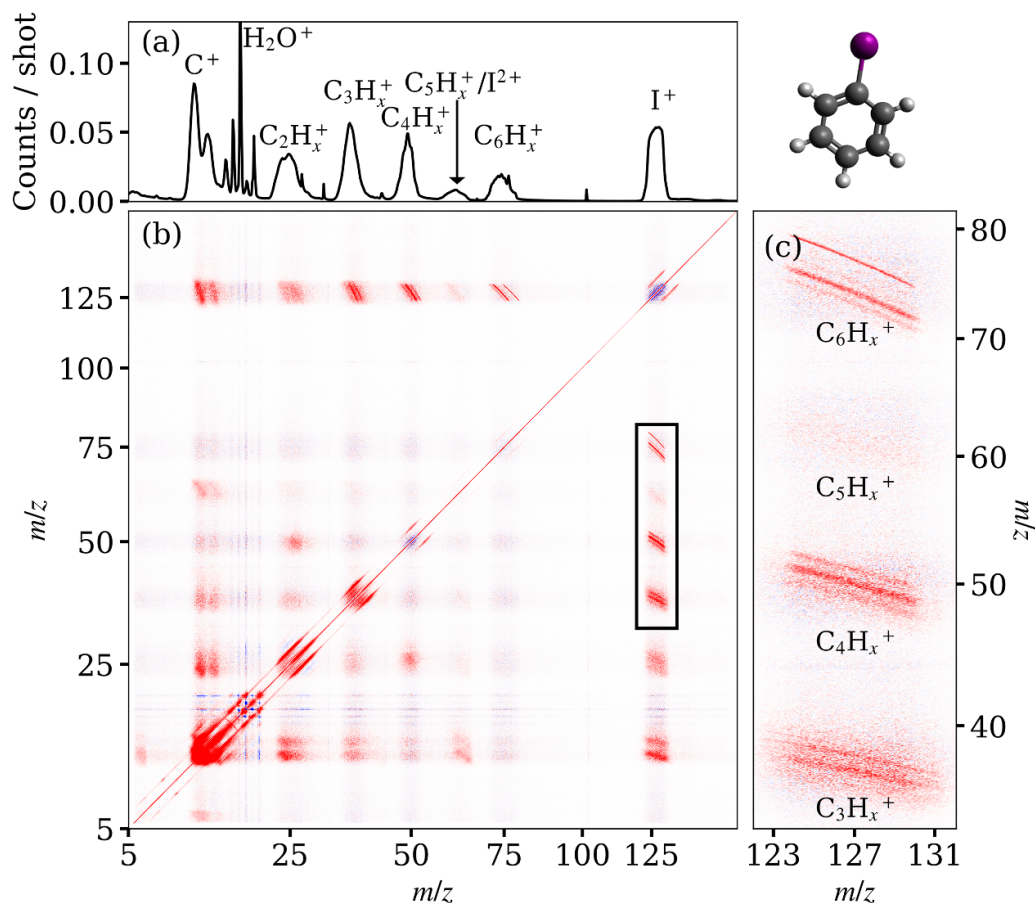
Figure 1. (a) The time-of-flight spectrum obtained following the XUV ionization of iodobenzene at 120 eV. (b) Time-of-flight covariances, calculated using 10 contingent covariance subsets. The region highlighted in the black box is magnified in (c) to illustrate covariances with high mass resolution between I^+ and various $C_nH_x^+$ fragments. Note the non-linear m/z scale applied to the time-of-flight data, starting at $m/z = 5$ as no meaningful covariance was observed at lower m/z values.

the secondary cation will be similar to the fraction expected from two-body conservation of momentum arguments (i.e., the $-m(C_nH_x^+)/m(C_6H_5^+)$ ratio). Any measured deviation from this expected ratio could indicate a greater kinetic energy release in the secondary dissociation step, but it is also worth noting that the time-of-flight covariance features in figure 1(c) can comprise contributions from the same pairs of ion species generated through competing fragmentation mechanisms or from different parent charge states, which could create a diffuse time-of-flight covariance feature due to the presence of overlapping signatures with different slopes. In any case, the deviations observed here between the experimentally determined time-of-flight covariance gradients and those predicted by (1) are relatively limited (less than 7%), so these effects are likely to be small.

More detailed descriptions of these fragmentation dynamics can be obtained by considering the relative momenta of the ions involved. For example, Coulomb explosions producing I^+ give rise to two distinct peaks at 153 ± 18 a.u. and 213 ± 26 a.u. in the I^+ momentum distribution, $p(I^+)$, as shown in figure 2(a). Figure 2(b) illustrates that these features are correlated with distinct groups of partner ions. For

example, when I^+ is covariant with $C_6H_2^+$, positive intensity is only observed in the lower-momentum range of the $p(I^+)$ distribution (red line). By contrast, both I^+ peaks are correlated with $C_6H_4^{2+}$ (blue line), which has the same m/z as $C_3H_2^+$. As will be detailed later, $C_6H_4^{2+}$ is associated with the higher momentum I^+ signal, due to its origin from a higher energy Coulomb explosion, while the $C_3H_2^+$ corresponds to the lower momentum peak. Furthermore, the $p(I^+)$ distribution obtained from three-fold covariance with $C_2H_2^+$ and $C_4H_2^+$ is also shown in figure 2(b) (black line). This distribution covers a similar range to the higher momentum I^+ signal in figure 2(a), indicating that I^+ can also be produced with two secondary ionic products. As a consequence, by applying momentum constraints to the I^+ data used in the covariance analysis, different fragmentation processes that generate I^+ can be distinguished and separately analyzed, as was demonstrated previously for the di- and trication fragmentation dynamics of 1- and 2-iodopropane [40, 50]. The following sections detail how this approach can be used in the case of iodobenzene to characterize fragmentation processes that generate I^+ and one carbon-containing monocation or I^+ with either a carbon-containing dication or two carbon-containing
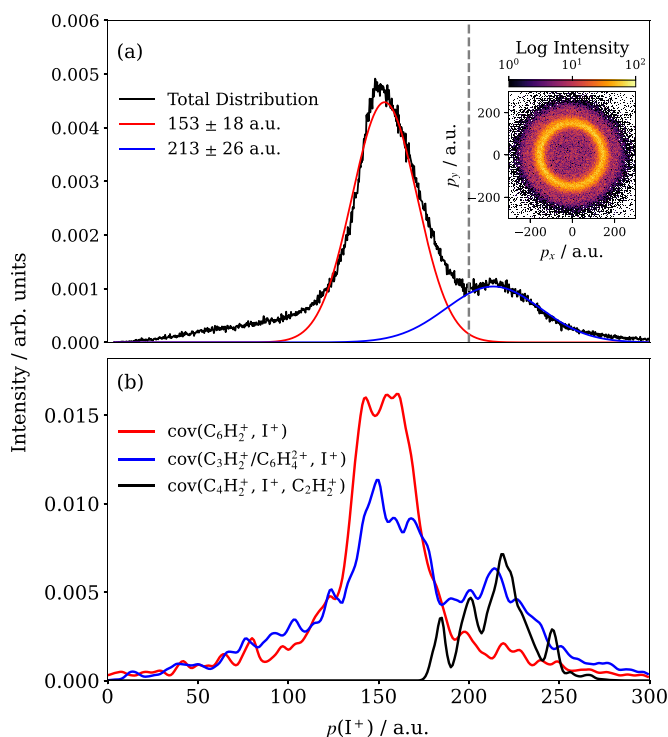
Figure 2. (a) The normalized I^+ momentum (p) distribution. Two peaks are evident and are modeled here by two Gaussian distributions to determine their centers and standard deviations, which are provided in the legend. The I^+ image used to produce this momentum distribution is also shown. The dashed grey line indicates the momentum ranges used to distinguish fragmentation mechanisms that contribute to these features by covariance analysis. (b) The normalized I^+ momentum distributions obtained via two-fold covariance with $C_6H_2^+$ (red) or $C_6H_4^{2+}/C_3H_2^+$ (blue), and via three-fold covariance with $C_4H_2^+$ and $C_2H_2^+$ (black), each of which have been independently normalized.
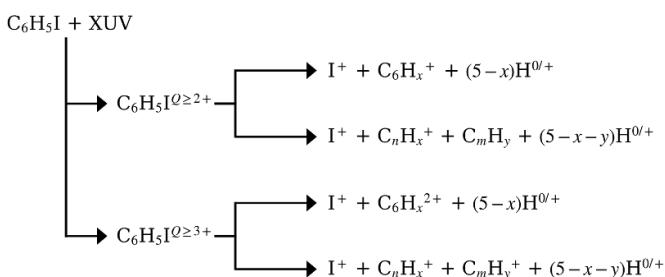

Figure 3. A summary of the four major categories of iodobenzene polycation fragmentation pathways discussed in this work, where Q is the total charge on the parent polycation, generated via XUV ionization, and $m + n = 6$.

cations. The potential reaction pathways are summarized in figure 3.

3.1. Processes generating I^+ and one $C_nH_x^+$

Fragmentation channels generating I^+ and one carbon-containing monocation are considered first. Such processes can be grouped into two categories: those producing $C_6H_x^+$

or those producing $C_nH_x^+$ ($n < 6$) with one or more neutral carbon-containing co-fragments. In either case, various amounts of H/H^+ loss were observed, which is likely due to a broad distribution of excited states being populated following interaction with the XUV pulse. The hydrocarbon ion momenta were observed to systematically change with increasing $H/H^+/C_nH_x$ loss. As will be shown in the following sections, this provides additional qualitative information on the behavior of these undetected species.

3.1.1. $I^+ + C_6H_x^+$. Reactions producing I^+ and $C_6H_x^+$ can be isolated using two-fold Newton-frame covariance analysis by restricting $p(I^+)$ to the lower momentum I^+ signal, as outlined above. Here, a limit of 200 a.u. was chosen (grey dashed line, figure 2(a)) as this retains virtually all of the signal in this channel while only introducing some overlap with the higher momentum feature, which originates from more highly-charged parent ions. This also ensures that the resulting momentum distributions of the covariant features are not unintentionally truncated, as they would be if a narrower $p(I^+)$ distribution were considered (further details for this choice can be found in section 4 of the supplementary material).

In the Newton-frame representation used here (e.g. figure 4(a)), the momentum of an ion of interest is plotted in the top half of the covariance map relative to the momentum of a reference ion (given by the white arrow). The momentum of any remaining mass of the molecule is then inferred through conservation of momentum and plotted in the bottom half of the covariance map. Figures 4(a) and (b) illustrate the momenta of $C_6H_5^+$ and $C_6H_2^+$ relative to I^+ as examples. It is worth noting that these were calculated using an angular constraint to remove false correlations arising from overlapping $C_6H_x^+$ Newton spheres, as described in section 5 and figure S4 of the supplementary material. The analogous Newton diagrams of the other $C_6H_x^+$ fragments can be found in section 6.1 and figure S5 of the supplementary material. In both maps, the recoil angles of the $C_6H_x^+$ momentum distributions are localized at 180° relative to I^+, indicating that The fragments recoil with equal and opposite momenta, as would be expected from the gradients observed in figure 1(b). In the case of $C_6H_2^+$, any impulse lost due to H/H^+ dissociation is small relative to that gained from the Coulomb explosion against I^+, due to the mass of hydrogen, but is sufficient to broaden the observed fragment angular distribution relative to the $C_6H_5^+$ feature.

The relative intensities of the covariance features observed for each $I^+/C_6H_x^+$ pair are provided in figure 4(c). These were obtained by integrating their respective features within their corresponding Newton frame representations. The error bars were obtained using the bootstrapping method described in the methods section, and represent the standard deviations of the averaged intensities. The greatest intensity is observed for $C_6H_2^+$, which is produced 41% ± 5% of the time in this channel, followed by $C_6H_5^+$ at 23% ± 5%. These values assume similar detection efficiencies for each ion, which is likely valid for small m/z ranges. The preference for multiple H/H^+ losses
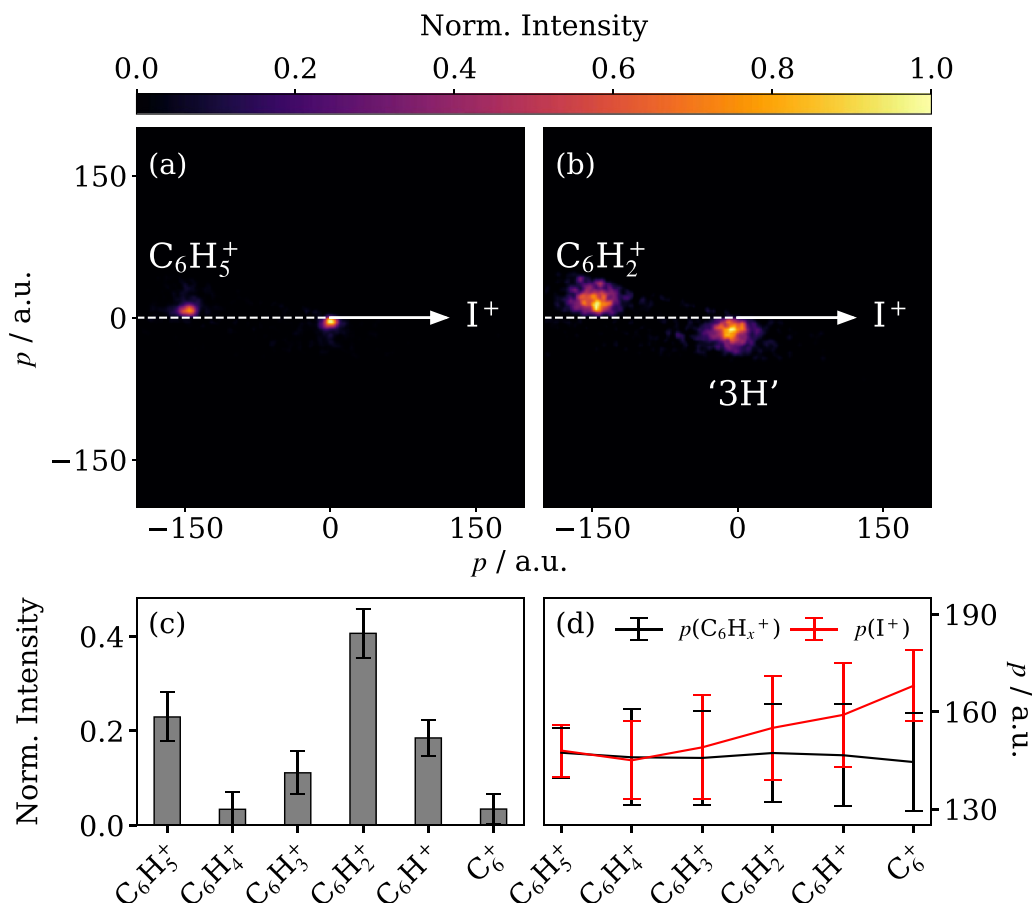
Figure 4. Individually normalized Newton-frame covariance maps showing the momentum distributions of $C_6H_5^+$ (a) and $C_6H_2^+$ (b) relative to I^+. Newton-frame covariance maps for all observed $C_6H_x^+$ fragments are provided in figure S5 of the supplementary material. The momenta of the $C_6H_x^+$ species are plotted in the top halves of each image. The inferred momenta of potential intact cofragments (if any) are inferred through momentum conservation arguments and plotted in the bottom halves. The inferred momentum in panel (a), which has no corresponding third fragment, corresponds to the 8 a.u. resolution of the experiment, as detailed in the main text. The relative integrated intensities of the covariance features between I^+ and each detected $C_6H_x^+$ ion are given in (c), and their average momentum values, obtained via Gaussian fitting, are given in (d). The error bars in (c) were determined using a bootstrapping method, where covariances were calculated for 100 subsets of data made up of 50 000 laser shots each. The error bars in (d) represent the Gaussian standard deviations of the momentum distributions.

suggests that the XUV interaction populates a range of highly-excited cationic states.

Figure 4(d) shows the mean momenta observed for the covariant $C_6H_x^+$ and I^+ pairs. These were determined by fitting the individual covariant $p(C_6H_x^+)$ and $p(I^+)$ momentum distributions with Gaussian functions to obtain central values and standard deviations. As the phenyl fragment becomes dehydrogenated, the momentum distributions of both ions broaden. The average I^+ momenta also increase by approximately 20 a.u. while the corresponding $C_6H_x^+$ momenta remain the same. These trends provide clues about the mechanisms involved in H/H^+ loss. If this occurred some time after the Coulomb explosion $p(I^+)$ would remain constant with changing x. However, if it occurred before the initial Coulomb explosion $p(I^+)$ could increase if the departing hydrogen atoms imparted momentum to the remaining molecule in the direction of the C–I bond. This latter trend in $p(I^+)$ is observed here, suggesting that H/H^+ loss may occur on a similar timescale to the C–I Coulomb explosion, such that $p(I^+)$ increases,

potentially due in part to electrostatic repulsion with H^+. Classical point charge Coulomb explosion simulations of this proposed mechanism, using the ground-state structure of neutral iodobenzene, can be found in section 6.2 of the supplementary material. These assume all hydrogen atoms are lost as H^+ for simplicity. The agreement in figure S6 between the measured and predicted $p(I^+)$ distributions supports the conclusion that H or H^+ loss can noticeably impact the momenta of the heavier fragments. However, it is worth noting that the assumption that all hydrogen species leave concertedly as H^+ represents a limiting case and that the actual distribution of mechanisms involved will be more complex. For instance, hydrogen could be lost sequentially from different carbon positions on the phenyl ring or in different sequences. It is also possible that some or all of the hydrogen species could be neutral or be lost on different timescales, including during the initial charge buildup caused by the Auger–Meitner process. The individual or combined effects of these potential mechanisms could contribute to the widths of the observed $p(C_6H_x^+)$

distributions as well as their discrepancies with these simulations. We note that in other studies where CH_3I has been ionized to very high charge states (e.g. up to 22+), small kinematic contributions from H or H^+ emission processes have been observed to influence the momenta of the resulting carbon and iodine ions [65, 66]. It is possible that a comparable effect is being observed here, despite the much lower iodine charge state.

3.1.2. $I^+ + C_nH_x^+$ ($n < 6$).

Next, fragmentation processes generating I^+, $C_nH_x^+$, and at least one neutral carbon-containing co-fragment are examined. Representative Newton-frame covariance maps showing the momentum distributions of $C_3H_2^+$ and $C_4H_3^+$ relative to I^+ are given in figures 5(a) and (b), respectively. In all cases involving this reaction channel, the covariance analysis only considered I^+ ions with $p(I^+) \leqslant 200$ a.u., as detailed above.

As in figure 4, the recoil angles observed in figures 5(a) and (b) are approximately 180°, indicating they are established primarily from the mutual Coulombic repulsion of the ions, with only negligible impulse imparted from the losses of the neutral co-fragments. Figure 5(c) exhibits the relative intensities of the covariances observed between I^+ and all $C_nH_x^+$ fragments that were sufficiently intense for covariance analysis. Their corresponding Newton-frame representations relative to I^+, calculated for all $p(I^+)$ as well as $p(I^+) \leqslant 200$ a.u. are also respectively collected in figures S7 and S8 of the supplementary material). The most prominent outcomes involved the production of $C_4H_x^+$ and $C_3H_x^+$. These occurred 44% ± 8% and 29% ± 7% of the time, respectively. We note that the preferential generation of $C_4H_x^+$ products has also been observed following the dissociative ionization of iodobenzene [32, 34].

To further investigate the mechanisms involved in producing the $C_nH_x^+$ fragments, it is again useful to consider their relative momenta. Figure 5(d) expresses these as a fraction of the corresponding I^+ momenta, $p(C_nH_x^+)/p(I^+)$. This quotient is related to the mass ratio $m(C_nH_x^+)/m(C_6H_5^+)$, which was introduced in (1) as an indicator for determining whether a reaction proceeds through an initial charge separation step followed by secondary dissociation. As such, if the covariant I^+ and $C_nH_x^+$ ion pairs were generated by such a mechanism, then the momentum and mass ratios given in the above equation should be approximately equal. Figure 5(d) illustrates that this is broadly true for the $C_nH_x^+$ fragments where $n = 4 - 5$. The momentum and mass ratios decrease together and are virtually identical, indicating that these ions were generated sequentially, with relatively little momenta added in the secondary dissociation step. However, as n decreases, the ratios increasingly deviate from each other, with greater $C_nH_x^+$ momenta than expected from a secondary dissociation. To demonstrate this change is statistically meaningful, the grey shaded regions in figure 5(d) indicate the uncertainties in the momentum ratios, as derived from the 8 a.u. momentum resolution of the instrument, while the error bars represent the Gaussian standard deviations of the momentum distributions, as shown in table S2 of the supplementary material [50]. For

the $C_2H_x^+$ and C^+ fragments, the mass ratios are just within the lower bounds of the uncertainty ranges determined from the standard deviations of the measured momentum distributions but are well below the ratios determined from their Gaussian centers. The origins of these ions are therefore likely to be more complex than those of the $C_5H_x^+$ and $C_4H_x^+$ species.

The mass-dependent deviations observed between the ratios plotted in figure 5(d) may simply be due to the fact that smaller $C_nH_x^+$ products with lower values of n can be generated through a larger number of fragmentation pathways [16, 23, 25]. For example, $C_2H_x^+$ can be formed with $C_4H_x^+$ via a two-body fragmentation of an intermediate, but can also be created from a many-body dissociation process where the intermediate breaks down into more than two products, or through tertiary fragmentation (e.g. $C_4H_3^+$ to C_2H^+ and C_2H_2). Alternatively, if these smaller products are generated on timescales that can be considered concerted with the initial C–I Coulomb explosion (i.e., a few femtoseconds), then their momenta will deviate from that expected from a sequential process. If smaller products are generated through a greater number of reaction pathways, then their momentum distributions will be broader. This effect may be captured here by the increase in the widths of the uncertainty ranges in figure 5(d) as n decreases.

In general, the momentum distributions of the covariant I^+ and $C_nH_x^+$ pairs where $n < 6$ are broader than the case where $n = 6$ (see table S2 as well as figures 4 and 5). This is likely due to blurring from H/H^+ loss as well as the existence of competing secondary fragmentation processes. As was the case for the $C_6H_x^+$ covariances, $p(I^+)$ increases with decreasing x. However, in contrast to the $C_6H_x^+$ momenta, which remained constant with x, the mean $p(C_nH_x^+)$ ($n < 6$) values also appear to increase with decreasing x. In this case, the x-dependence of the $C_nH_x^+$ fragment momenta may be a result of the lower masses of the $C_6H_x^+$ ($x < 5$) intermediates relative to $C_6H_5^+$.

The relative intensities of the covariances observed from the fragmentation channels producing I^+ and one carbon-containing cation $C_nH_x^+$ ($n = 2 - 6$) are expressed as percentages of all observable covariances of this type in table 1. As was shown in figures 4 and 5, the most prominent outcomes are the $C_4H_2^+$, $C_6H_2^+$, and C_3H^+ fragments. This indicates that, more often than not, the $C_nH_x^+$ fragments are sufficiently activated following C–I cleavage to undergo H/H^+ loss or further fragmentation. Approximately 20% ± 4% of intermediates are internally excited enough to undergo H/H^+ loss to form $C_6H_x^+$ ($x < 5$) products, while 73% ± 10% undergo carbon-chain fragmentation to form $C_nH_x^+$ ($n < 6$). At least 64% ± 9% of intermediates exhibit hydrogen loss in addition to carbon-chain fragmentation (forming $C_nH_x^+$ products where $n < 6$ and $x < n$).

The wide range of products measured is likely a result of generating many different $C_6H_x^+$ intermediates, which could exist long enough for structural distortions to occur before secondary dissociation. Theoretical studies have proposed minimum-energy configurations of the secondary $C_nH_x^+$ products observed here [8]. For example, $C_3H_3^+$ and $C_5H_x^+$ are expected to be cyclic, while $C_4H_x^+$ and $C_2H_2^+$ are likely
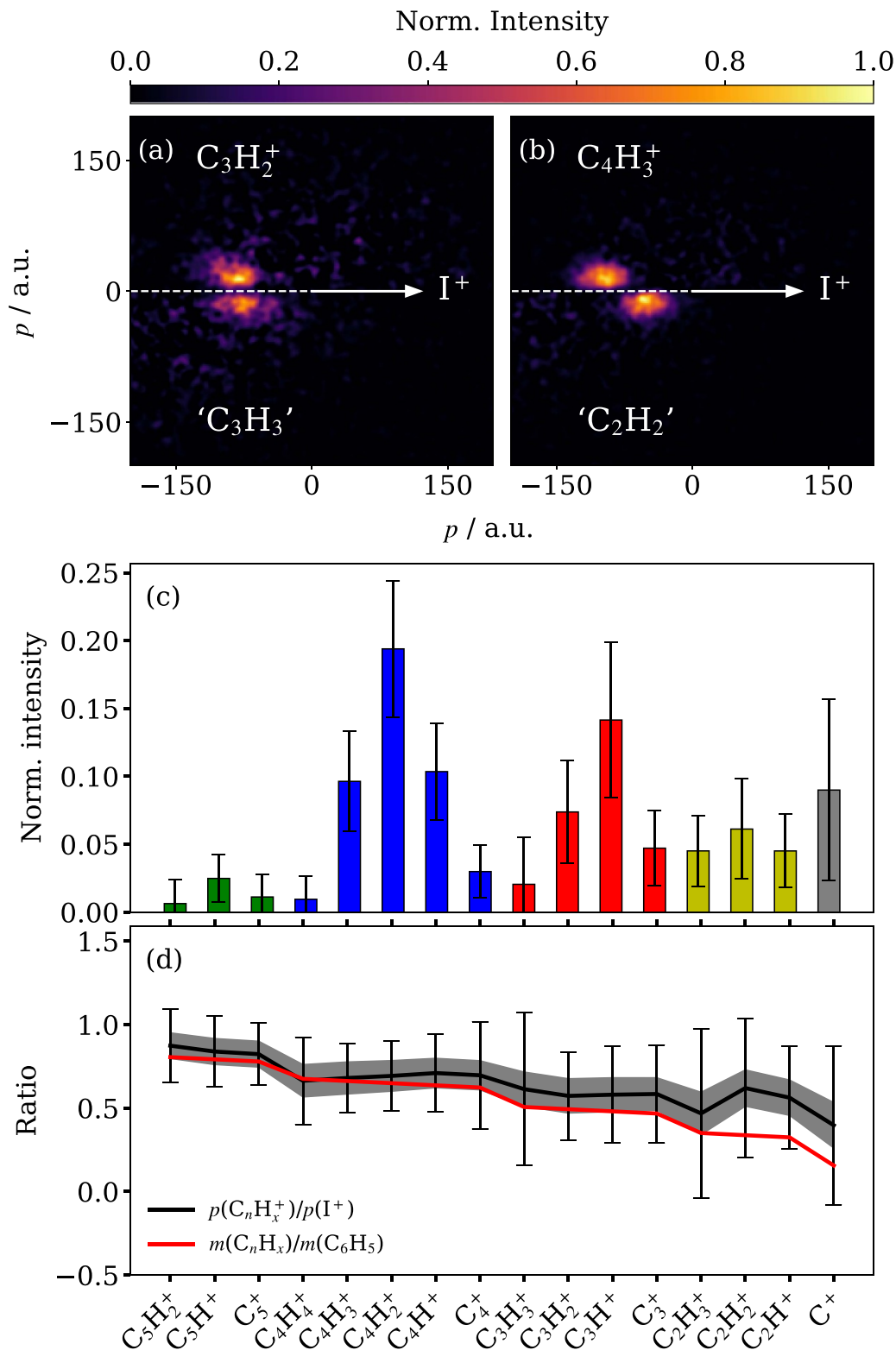
Figure 5. Independently normalized Newton-frame covariance maps showing the momentum distributions of $C_3H_2^+$ (a) and $C_4H_3^+$ (b) relative to I^+ with $p(I^+)$ filtered to 200 a.u. or less. Newton-frame covariance maps for all $C_nH_x^+$ species with $n < 6$ are provided in figure S8 of the supplementary material. The relative integrated intensities of the covariance features between I^+ and each detected $C_nH_x^+$ ion are given in (c), with error bars obtained using the bootstrapping method. In (d), the momentum ratios of the charged fragments $p(C_nH_x^+)/p(I^+)$ are compared with the mass ratios $m(C_nH_x)/m(C_6H_5)$ (as in (1)). The grey shaded region corresponds to the uncertainty inherent in the average momentum values due to the instrument resolution, while the error bars were determined using the Gaussian standard deviations of the $C_nH_x^+$ and I^+ momentum distributions.

Table 1. Relative normalized intensities for the fragmentation channels producing I^+ and one $C_nH_x^+$ ($n = 2-6$), as determined from the covariance data in figures 4(c) and 5(c). The uncertainties are calculated using the bootstrapping method described in the supplementary material.

Fragment	Intensity (%)	Fragment	Intensity (%)	Fragment	Intensity (%)
$C_6H_5^+$	8 ± 2	$C_5H_2^+$	1 ± 1	$C_3H_3^+$	1 ± 3
$C_6H_4^+$	1 ± 2	C_5H^+	2 ± 1	$C_3H_2^+$	6 ± 3
$C_6H_3^+$	3 ± 2	C_5^+	1 ± 1	C_3H^+	10 ± 3
$C_6H_2^+$	11 ± 2	$C_4H_4^+$	1 ± 1	C_3^+	4 ± 2
C_6H^+	5 ± 2	$C_4H_3^+$	7 ± 2	$C_2H_3^+$	3 ± 2
C_6^+	1 ± 2	$C_4H_2^+$	14 ± 4	$C_2H_2^+$	5 ± 2
		C_4H^+	7 ± 2	C_2H^+	3 ± 2
		C_4^+	2 ± 2	C^+	6 ± 4

to be more linear. Forming cyclic products within the lifetime of a $C_6H_x^+$ intermediate would potentially require ring opening and closing mechanisms and atom re-arrangement. The intermediate species generating each of these products are unlikely to all be in their electronic or vibrational ground states, so it cannot be assumed that the secondary products will also be formed in their predicted lowest energy configurations. Furthermore, the very broad momentum distributions observed here suggest that, for each $C_nH_x^+$ species, a range of products are formed with different internal excitation and, possibly, different geometries.

3.2. Processes generating I^+ and one $C_nH_x^{2+}$ or two carbon-containing monocations

The following sections consider fragmentation channels that generate I^+ with either $C_6H_x^{2+}$ or two carbon-containing monocations, $C_nH_x^+$ and $C_{(6-n)}H_y^+$. As before, various degrees of H/H^+ loss are observed in both cases.

3.2.1. $I^+ + C_6H_x^{2+}$.
The mass-to-charge ratio of $C_6H_x^{2+}$ overlaps with that of $C_3H_x^+$. To isolate the former, the covariance analysis was restricted to I^+ products with 200 a.u. of momenta or greater (see figure 2). Figures 6(a) and (b) illustrate the Newton-frame momentum plots of $C_6H_5^{2+}$ and $C_6H_2^{2+}$ relative to I^+. The corresponding Newton diagrams of the other $C_6H_x^{2+}$ fragments that are covariant with I^+ are shown in figure S9 of the supplementary material. Their distributions are similar to those observed in figure 4, where I^+ and the $C_6H_x^+$ fragments exhibited back-to-back recoil, although it should be noted that the $C_6H_x^{2+}$ momentum distributions are slightly truncated due to the 200 a.u. bound mentioned above. This similarity extends to the effective charge separation prior to fragmentation, as determined by Coulomb's law. For example, the relative momenta of I^+ and $C_6H_5^{2+}$ suggest a charge separation of 4.2 ± 0.2 Å, which is close to the 4.3 ± 0.3 Å separation determined for the Coulomb explosion of I^+ and $C_6H_5^+$. This indicates that the fragments originate from similar nuclear geometries, assuming that the Coulomb explosion is prompt. Section 8 of the supplementary material

demonstrates that the analogous $C_6H_x^{+/2+}$ ($x = 2-4$) fragment pairs behave similarly.

Figure 6(c) shows the normalized relative intensities of the covariances observed between I^+ and the $C_6H_x^{2+}$ ($x = 2-5$) fragments (no correlations involving C_6H^{2+} or C_6^{2+} were observed). Similar to the $C_6H_x^+$ reaction channels, the greatest observed intensities suggest that the XUV interaction preferentially generates states that undergo H/H^+ loss. However, it should be noted that all of the $C_6H_x^{2+}$ covariance magnitudes are within error of each other, and there is much less disparity between them than was observed for the $C_6H_x^+$ fragments (figure 4(c)). Figure 6(d) illustrates how the relative momenta of the species produced in this fragmentation channel change with decreasing hydrogenation. Similar to the $C_6H_x^+$ fragments (figure 4(d)), H/H^+ loss has a negligible effect on the average $C_6H_x^{2+}$ momenta, while the I^+ momenta are, again, seen to increase. The widths of the $p(C_6H_x^{2+})$ and $p(I^+)$ distributions also broaden as x decreases. The similar trends observed for the processes generating $C_6H_x^+$ and $C_6H_x^{2+}$ add weight to the conclusion that H/H^+ loss is fast relative to C–I bond cleavage and that it occurs on timescales faster than the geometrical distortions of the carbon ring.

3.2.2. $I^+ + C_nH_x^+ + C_{(6-n)}H_y^+$.
For fragmentation channels producing I^+ and two carbon-containing monocations ($C_nH_x^+$ and $C_{(6-n)}H_y^+$, with varying degrees of H/H^+ loss), the corresponding covariance features were again isolated by only considering I^+ products with $p \geqslant 200$ a.u. in the analysis. Figures 7(a) and (b) exhibit two representative Newton-frame covariance maps from the Coulomb explosion of iodobenzene into I^+, $C_2H_2^+$, and $C_4H_x^+$ as examples of the fragmentation dynamics that can occur in this reaction channel. In the first, the momentum of $C_2H_2^+$ is shown relative to I^+, with the distribution of '$C_4H_3^+$' inferred as a putative cofragment (assuming a purely three-body fragmentation mechanism and neglecting H/H^+ loss processes). The $C_2H_2^+$ distribution spans a broad range of recoil angles, which is characteristic of a sequential three-body breakup [40, 67, 68]. In this case, a primary Coulomb explosion forms I^+ and an unstable $C_6H_x^{2+}$ intermediate, which undergoes a secondary Coulomb explosion at a later time to produce $C_2H_2^+$
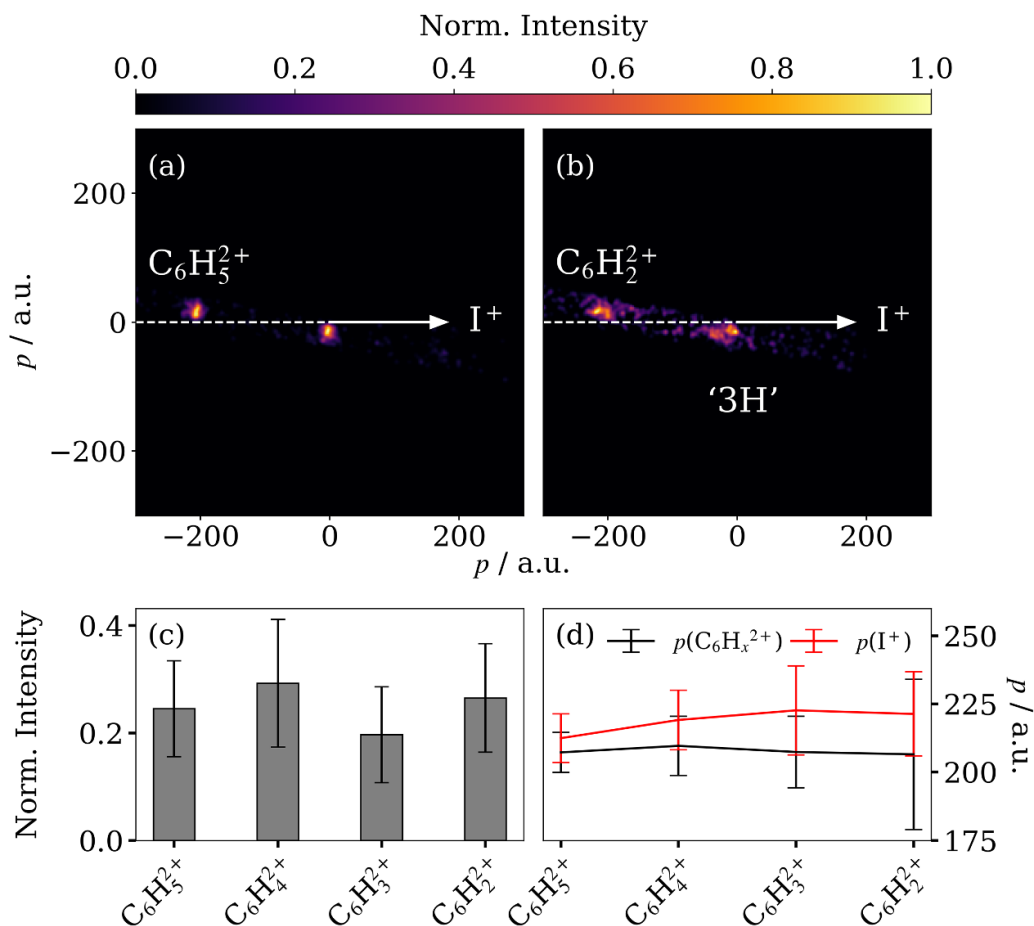
J. Phys. B: At. Mol. Opt. Phys. **57** (2024) 235101

T Walmsley *et al*

Figure 6. Individually normalized Newton-frame covariance maps showing the momentum distributions of $C_6H_5{}^{2+}$ (a) and $C_6H_2{}^{2+}$ (b) relative to I^+. Newton-frame covariance maps for all $C_6H_x{}^{2+}$ species are given in figure S9 of the supplementary material. The relative integrated intensities of the covariance features are given in (c), with error bars determined through the bootstrapping method. The average momentum values obtained for all correlated $C_6H_x{}^{2+}$ and I^+ fragments are given in (d), along with error bars that correspond to their Gaussian standard deviations.

and '$C_4H_3{}^+$'. Since the intermediate exists long enough to rotate significantly, the resulting trajectories of the carbon-containing fragments sweep out broad angular distributions relative to I^+. Moreover, the same secondary products can be formed from different non-equivalent sites on the intermediate relative to the original C–I bond, which further contributes to the angular extent of the distribution. By contrast, in figure 7(b), the distribution of $C_2H_2{}^+$ is now shown relative to $C_4H_2{}^+$ with a combination of I^+ and H/H^+ as the inferred third species. Here, the secondary products predominantly recoil near 180°, indicating they originate from the same intermediate.

To analyze the secondary Coulomb explosion of $C_6H_x{}^{2+}$ independently of the primary Coulomb explosion, a covariant native frames approach was implemented [40]. This removes the momentum contributed by the I^+ fragments, enabling figure 7(a) to be transformed into figure 7(c), where the relative momenta of the secondary products are now shown in the isolated reference frame of the $C_6H_x{}^{2+}$ intermediate. The distribution is also given in polar coordinates in figure 7(d), showing that the angular distribution is essentially

isotropic. This implies that $C_2H_2{}^+$ is produced in a sequential fragmentation process, as the $C_6H_x{}^{2+}$ must at least exist long enough to complete a full rotational period [67]. In this representation, it can also be seen that the carbon-fragment momenta are essentially independent of the recoil angle, again indicating they originate from a relatively long-lived intermediate. That being said, the momentum distributions are rather broad, which is likely a result of products being generated from several similar excited states with slightly different geometries, degrees of dehydrogenation, or intermediate lifetimes.

Similar correlations to those shown in figures 7(a)–(d) could be distinguished for a range of $C_nH_x{}^+$ species where $n = 2-5$. These are provided in figure S10 of the supplementary material. Using this output, the I^+ momenta corresponding to the generation of several intermediary $C_6H_x{}^{2+}$ species were determined. These are compared in table S3 of the supplementary material, alongside the values observed when the $C_6H_x{}^{2+}$ cofragment remains intact. The I^+ momenta are effectively the same, with an average of 222 ± 4 a.u. across all fragmentation channels, where the uncertainty is the standard deviation
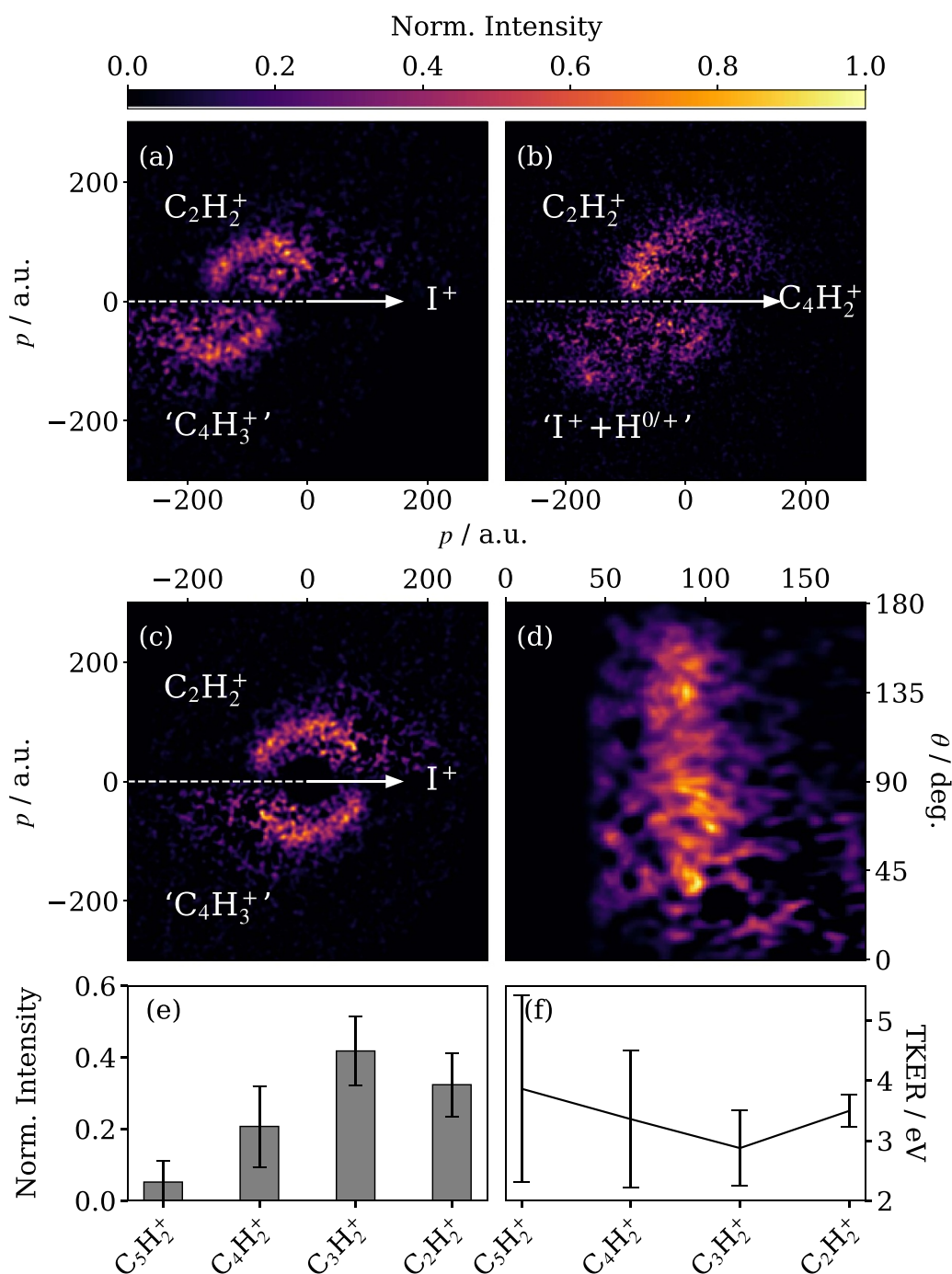
Figure 7. Individually normalized Newton-frame covariance maps showing the momentum distributions of $C_2H_2{}^+$ relative to I^+ ($p(I^+) \geqslant 200$ a.u.) and $C_4H_2{}^+$ are given in (a) and (b), respectively. The former distribution is adapted into the native frame of the phenyl dication intermediate in (c) and as a polar representation in (d). The relative integrated intensities obtained for the native-frame covariant features involving I^+ and $C_nH_x{}^+$ are given in (e), with error bars obtained through the bootstrapping method. The corresponding native-frame covariance maps for these $C_6H_x{}^+$ species are given in figure S10 of the supplementary material. The approximate total kinetic energies released (TKER) by the secondary Coulomb explosion channels of the phenyl dication are provided in (f), with error bars derived from the Gaussian standard deviations of the momentum distributions.

of the mean. This suggests that the primary Coulomb explosion processes are broadly similar. The integrated intensities of the secondary Coulomb explosion fragments that are covariant with I^+ are shown in figure 7(e). The most probable fragmentation channels generate either $C_4H_x{}^+$ and $C_2H_y{}^+$ or $C_3H_x{}^+$ and $C_3H_y{}^+$ co-products. This agrees with previous studies on

the benzene dication, which demonstrated that $C_6H_6{}^{2+}$ preferentially fragments into products with even numbers of carbons (e.g, $C_4H_3{}^+ + C_2H_3{}^+$) [69].

The secondary $C_nH_x{}^+$ fragment momenta measured using the native frames of the $C_6H_x{}^{2+}$ intermediates are similar to those observed for the fragmentation of the benzene

Table 2. The total fragment kinetic energies released (TKER) from secondary Coulomb explosions that form $C_nH_x^+$ and $C_{6-n}H_y^+$ (where $x + y \leqslant 5$). Approximate values summed from two-fold covariances of these fragments with respect to I^+ (i), assuming $y = (6-n)-1$, as well as directly from three-fold covariances between I^+, $C_nH_x^+$, and $C_{6-n}H_y^+$ (ii) are provided, along with the expected intercharge separations (r). The uncertainties correspond to the Gaussian standard deviations of the covariant ion momentum distributions.

	Fragments	TKER (eV)	r (Å)
(i)	$C_5H_2^+ + C^+$	3.9 ± 1.6	3.7 ± 1.5
	$C_4H_2^+ + C_2H^+$	3.3 ± 1.1	4.4 ± 1.5
	$C_3H_2^+ + C_3H_2^+$	2.9 ± 0.6	5.0 ± 1.0
	$C_2H_2^+ + C_4H_3^+$	3.5 ± 0.3	4.1 ± 0.4
(ii)	$C_4H_3^+ + C_2H_2^+$	3.8 ± 0.1	3.8 ± 0.1
	$C_4H_2^+ + C_2H_2^+$	3.8 ± 0.1	3.8 ± 0.1
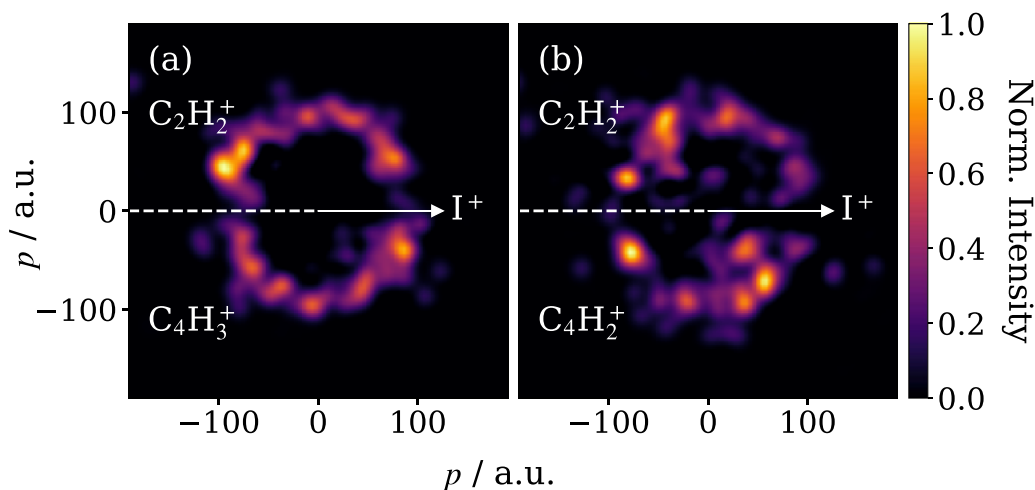
Figure 8. Three-fold native-frame covariance maps showing the momenta of (a) $C_2H_2^+$ and $C_4H_3^+$ relative to I^+ and (b) $C_2H_2^+$ and $C_4H_2^+$ relative to I^+. A Gaussian blur has been applied to both covariance maps to enhance the visibility of the features. Analogous images without this adjustment can be found in figure S11 of the supplementary material.

dication at 40.8 eV. For example, Eland and coworkers previously reported product pairs of carbon-containing cations (and neutral hydrogen) with the following total kinetic energy releases [69]:

$$C_5H_2^+ + CH_3^+ + H = 3.0 \pm 1.7 \, eV$$
$$C_4H_3^+ + C_2H_2^+ + H = 3.8 \pm 1.0 \, eV$$
$$C_3H_2^+ + C_3H_3^+ + H = 4.2 \, eV.$$
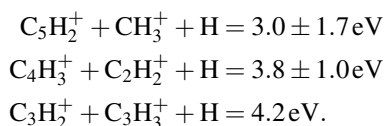
They also observed that the kinetic energy released by different $C_nH_x^+/C_{6-n}H_y^+$ pairs did not depend on the number of hydrogen atoms involved, suggesting that the parent geometries were similar and that the hydrogen atoms were lost as neutrals.

As a comparison, the secondary Coulomb explosion fragment kinetic energies for various $C_nH_x^+/C_{6-n}H_y^+$ ($x+y \leqslant$ 5) pairs were determined here using the native-frame results. Approximate kinetic energy values were first estimated from the two-fold $I^+/C_nH_x^+$ covariance distributions using the approximation $y = (6-n)-1$ (i.e., there is one less hydrogen than carbon in the $C_{6-n}H_y^+$ co-fragment). This simplification was made as the effects of H/H^+-loss on the

momenta of the carbon-containing products should essentially be negligible, and because the uncertainties they add are captured by the widths of the ion momentum distributions. These approximate energies are given in table 2(i) and are plotted in figure 7(f). Table 2 also provides the corresponding separations (r) between the charges on the dicationic intermediates prior to their fragmentation, as determined using Coulomb's law for an instantaneous explosion.

To verify the approximate kinetic energies obtained from the two-fold covariance maps, three-fold native-frame covariances were also calculated for two sets of ions: I^+, $C_2H_2^+$, and $C_4H_3^+$; as well as I^+, $C_2H_2^+$, and $C_4H_2^+$. These are shown in figures 8(a) and (b), respectively. The fragmentation mechanisms producing other sets of fragment ions were too low in intensity to yield converged three-fold covariance maps. In figure 8(b), one H/H^+ is unaccounted for. However, the small difference in mass due to the lost H/H^+ does not significantly alter the measured fragment energies, as expected. The TKER from both sets of ions are given in table 2(ii), along with their corresponding charge separations, and are in strong agreement with each other as well as the values estimated from the two-fold covariances, indicating that the $y = (6-n)-1$ assumption is reasonable.

The similarities between the kinetic energies released by the $C_6H_x^{2+}$ intermediates following core ionization at 120 eV (table 2), and those measured for the double ionization and fragmentation of the benzene dication at 40.8 eV, suggest that, as expected, these species are structurally similar [69]. However, it is worth noting that in the latter case, the dications fragmented promptly and no intermediates were observed [69]. By contrast, the higher photon energy used in these experiments appears to result in a multitude of $C_6H_x^{2+}$ states being populated, which persist long enough before fragmentation to be detectable. Therefore, it is reasonable to conclude that extensive structural re-arrangements could occur prior to the secondary Coulomb explosion process. For example, Anand and Schlegel computed theoretical potential energy surfaces for the fragmentation of benzene dications into two charged species, which demonstrated a range of linear and cyclic products could be accessible [8]. Based on their predicted geometries and our experimentally obtained intercharge separations, as shown in table 2, we anticipate that the geometries of the $C_6H_x^{2+}$ intermediates are most likely distorted cyclic structures, not so far from the structure of neutral phenyl, which then fragment into somewhat linear secondary products. However, the broad momentum distributions observed here do not rule out contributions from other pathways.

4. Conclusions

Newton-frame covariance analysis was used to distinguish and categorize the primary and secondary fragmentation dynamics of iodobenzene. Site-selective iodine 4d ionization at 120 eV was used to produce highly-charged parent ions through the Auger–Meitner effect. These primarily broke apart at the carbon-iodine bond to produce I^+ with $C_nH_x^+$ or $C_nH_x^{2+}$ products with different extents of dehydrogenation. The hydrocarbon products were generated in a range of stable and unstable states, frequently with enough internal energy to lose neutral carbon-containing products. Furthermore, the momentum and angular distributions of these secondary fragmentations often indicated that the C_6H_x intermediates can exist long enough to complete full rotational periods. These observations enabled the dynamics of several phenyl and phenyl-like cations to be examined, particularly by using the native frames of the $C_6H_x^{2+}$ intermediates. The roughly 1 Da resolution of the VMI spectrometer further allowed these reaction channels to be differentiated at the level of individual hydrogen atoms, which provided a comprehensive picture of the distribution of competing fragmentation channels, including those of the hydrocarbon intermediates.

The ability of covariance analysis to detail the competing fragmentation dynamics of aryl polycations demonstrates proof of principle for extending these methods to characterize the XUV-induced chemistry of more complex species. For example, PAHs are likely to be excellent targets for this approach. The time-resolved XUV-induced dynamics of several PAHs, including fluorene, phenanthrene, and pyrene, have previously been shown to result in the loss of neutral hydrogen atoms or acetylene, and the techniques presented here could

provide additional information on the intermediate steps of such reactions and how they depend on the hydrogenation of the carbon skeleton [23, 25].

The results presented here also indicate that some degree of caution is required when interpreting the outcomes of XUV-induced Coulomb explosions originating from lowly-charged parent ions, particularly their use for structural imaging. The application of Coulomb explosion imaging for molecular structural determination relies on reaching high charge states, such that fragmentation occurs immediately after ionization and the fragment momenta provide 'instantaneous' snapshots of the nuclear geometry. However, as was detailed above, the ionization of many-atom systems can generate relatively large mono- or dications that can persist for some time before fragmenting. The lack of sensitivity to the wide range of possible H/H^+-loss processes, which may occur on timescales competitive with Auger–Meitner charge generation, can also result in incomplete characterizations of the fragmentation dynamics, particularly for organic compounds. It is therefore important to be able to recognize and interpret such outcomes when using XUV-induced Coulomb explosions as a structural probe, and the techniques presented here provide a potential route for meeting this challenge.

Data availability statement

All data that support the findings of this study are included within the article (and any supplementary files).

Acknowledgments

ORCID iDs

Tiffany Walmsley ● https://orcid.org/0000-0002-1446-5904
Felix Allum ● https://orcid.org/0000-0002-8044-8969
Yoshiaki Kumagai ● https://orcid.org/0000-0002-2492-4676
Mark Brouard ● https://orcid.org/0000-0003-3421-0850
Mizuho Fushitani ● https://orcid.org/0000-0002-1683-0178
Ian Gabalski ● https://orcid.org/0000-0002-6782-6566
Tatsuo Gejo ● https://orcid.org/0000-0002-7191-4999
Paul Hockett ● https://orcid.org/0000-0001-9561-8433
Andrew J Howard ● https://orcid.org/0000-0003-0303-3222
Hiroshi Iwayama ● https://orcid.org/0000-0002-5992-5281
Chow-shing Lam ● https://orcid.org/0000-0002-4296-7944
Russell S Minns ● https://orcid.org/0000-0001-6775-2977
Akinobu Niozu ● https://orcid.org/0000-0002-7292-5630
Sekito Nishimuro ● https://orcid.org/0009-0002-2766-3122
Shigeki Owada ● https://orcid.org/0000-0002-1451-7612
Daniel Rolles ● https://orcid.org/0000-0002-3965-3477
James Somper ● https://orcid.org/0009-0008-7942-5576
Ruaridh Forbes ● https://orcid.org/0000-0003-2097-5991
Michael Burt ● https://orcid.org/0000-0002-7317-8649
Emily M Warne ● https://orcid.org/0000-0002-1205-6939

References

[1] Slegt M, Overkleeft H S and Lodder G 2007 *Fingerprints of Singlet and Triplet Phenyl Cations* (Wiley)
[2] Dichiarante V, Protti S and Fagnoni M 2017 *J. Photochem. Photobiol.* A **339** 103–13
[3] Torrisi S and Sortino S 2004 *J. Agric. Food Chem.* **52** 5943–9
[4] Fasani E, Profumo A and Albini A 1998 *Photochem. Photobiol.* **68** 666–74
[5] Tasaka M, Ogata M and Ichikawa H 1981 *J. Am. Chem. Soc.* **103** 1885–91
[6] Krogh-Jespersen K 1991 *J. Am. Chem. Soc.* **113** 417–23
[7] Harvey J N, Aschi M, Schwarz H and Koch W 1998 *Theor. Chem. Account.* **99** 95–99
[8] Anand S and Schlegel H B 2005 *J. Phys. Chem.* A **109** 11551–9
[9] Jasik J, Gerlich D and Roithová J 2014 *J. Am. Chem. Soc.* **136** 2960–2
[10] Galbraith M C E *et al* 2017 *Nat. Commun.* **8** 1018
[11] Bazzi S, Welsch R, Vendrell O and Santra R 2018 *J. Phys. Chem.* A **122** 1004–10
[12] Wiersma S D, Candian A, Bakker J M, Berden G, Eyler J R, Oomens J, Tielens A G G M and Petrignani A 2021 *Phys. Chem. Chem. Phys.* **23** 4334–43
[13] Allamandola L J, Tielens A G G M and Barker J R 1989 *Astrophys. J. Suppl. Ser.* **71** 733–75
[14] Lagache G *et al* 2004 *Astrophys. J. Suppl. Ser.* **154** 112
[15] Joblin C and Tielens A G G M 2011 *Eur. Astron. Soc. Publ. Ser.* **46** 3–10
[16] Leach S, Eland J H D and Price S 1989 *J. Phys. Chem.* **93** 7583–93
[17] Champeaux J P, Moretto-Capelle P, Cafarelli P, Deville C, Sence M and Casta R 2014 *Mon. Not. R. Astron. Soc.* **441** 1479–87
[18] Reitsma G, Boschman L, Deuzeman M J, Hoekstra S, Hoekstra R and Schlathölter T 2015 *J. Chem. Phys.* **142** 024308
[19] Marciniak A *et al* 2015 *Nat. Commun.* **6** 7909
[20] Zhen J, Castillo S R, Joblin C, Mulas G, Sabbah H, Giuliani A, Nahon L, Martin S, Champeaux J P and Mayer P M 2016 *Astrophys. J.* **822** 113
[21] Bagdia C, Biswas S, Mandal A, Bhattacharjee S and Tribedi L C 2021 *Eur. Phys. J.* D **75** 1–7
[22] Boyer A, Hervé M, Despré V, Nash P C, Loriot V, Marciniak A, Tielens A G G M, Kuleff A I and Lépine F 2021 *Phys. Rev.* X **11** 041012
[23] Lee J W L *et al* 2021 *Nat. Commun.* **12** 6107
[24] Lee J W L *et al* 2022 *Phys. Chem. Chem. Phys.* **24** 23096–105
[25] Garg D *et al* 2022 *Front. Phys.* **10** 880793
[26] Ehrenfreund P and Sephton M A 2006 *Faraday Discuss.* **133** 277–88
[27] Tielens A G G M 2008 *Annu. Rev. Astron. Astrophys.* **46** 289–337
[28] Herbst E and Van Dishoeck E F 2009 *Annu. Rev. Astron. Astrophys.* **47** 427–80
[29] Chandler D W and Houston P L 1987 *J. Chem. Phys.* **87** 1445–7
[30] Eppink A T J B and Parker D H 1997 *Rev. Sci. Instrum.* **68** 3477–84
[31] Forbes R *et al* 2020 *J. Phys. B: At. Mol. Opt. Phys.* **53** 224001
[32] Dannacher J, Rosenstock H M, Buff R, Parr A C, Stockbauer R L, Bombach R and Stadelmann J P 1983 *Chem. Phys.* **75** 23–35
[33] Malinovich Y and Lifshitz C 1986 *J. Phys. Chem.* **90** 2200–3
[34] Newton K R and Bernstein R B 1983 *J. Phys. Chem.* **87** 2246–55
[35] Holmegaard L, Nielsen J H, Nevo I, Stapelfeldt H, Filsinger F, Küpper J and Meijer G 2009 *Phys. Rev. Lett.* **102** 023001
[36] Erk B *et al* 2013 *Phys. Rev. Lett.* **110** 053003
[37] Rudenko A *et al* 2017 *Nature* **546** 129–32
[38] Fukuzawa H and Ueda K 2020 *Adv. Phys.* X **5** 1785327
[39] Boll R *et al* 2022 *Nat. Phys.* **18** 423–8
[40] McManus J W *et al* 2022 *Phys. Chem. Chem. Phys.* **24** 22699–709
[41] Li X *et al* 2022 *Phys. Rev. Res.* **4** 013029
[42] Frasinski L J, Codling K and Hatherly P A 1989 *Science* **246** 1029–31
[43] Slater C S *et al* 2014 *Phys. Rev.* A **89** 011401
[44] Slater C S, Blake S, Brouard M, Lauer A, Vallance C, Bohun C S, Christensen L, Nielsen J H, Johansson M P and Stapelfeldt H 2015 *Phys. Rev.* A **91** 053424
[45] Allum F, Cheng C, Howard A J, Bucksbaum P H, Brouard M, Weinacht T and Forbes R 2021 *J. Phys. Chem. Lett.* **12** 8302–8
[46] Vallance C, Heathcote D and Lee J W L 2021 *J. Phys. Chem.* A **125** 1117–33
[47] Minion L, Lee J W L and Burt M 2022 *Phys. Chem. Chem. Phys.* **24** 11636–45
[48] Fukuzawa H, Nagaya K and Ueda K 2018 *Nucl. Instrum. Methods Phys. Res.* A **907** 116–31
[49] Rajput J *et al* 2018 *Phys. Rev. Lett.* **120** 103001
[50] Walmsley T *et al* 2024 *J. Phys. Chem.* A **128**
[51] Tono K *et al* 2013 *New J. Phys.* **15** 083035

[52] Auger P 1975 *Surf. Sci.* **48** 1–8
[53] Olney T N, Cooper G and Brion C 1998 *Chem. Phys.*
      232 211–37
[54] Yeh J J and Lindau I 1985 *At. Data Nucl. Data Tables*
      32 1–155
[55] Owada S, Fushitani M, Matsuda A, Fujise H, Sasaki Y,
      Hikosaka Y, Hishikawa A and Yabashi M 2020 *J.
      Synchrotron Radiat.* **27** 1362–5
[56] Owada S *et al* 2018 *J. Synchrotron Radiat.* **25** 282–8
[57] Frasinski L J 2016 *J. Phys.* B **49** 152004
[58] Pickering J D, Amini K, Brouard M, Burt M, Bush I J,
      Christensen L, Lauer A, Nielsen J H, Slater C S and
      Stapelfeldt H 2016 *J. Chem. Phys.* **144** 161105
[59] Zhaunerchyk V, Frasinski L J, Eland J H D and Feifel R 2014
      Phys. Rev. A **89** 053418

[60] Mucke M *et al* 2015 *New J. Phys.* **17** 073002
[61] Heathcote D and Vallance C 2021 *J. Phys. Chem.* A
      125 7092–8
[62] Unwin J *et al* 2023 *Commun. Phys.* **6** 309
[63] Eland J H D 1987 *Mol. Phys.* **61** 725–45
[64] Kukk E, Pihlava L, Kooser K, Stråhlman C, Maclot S and
      Kivimäki A 2023 *Phys. Chem. Chem. Phys.* **25** 5795–807
[65] Motomura K *et al* 2015 *J. Phys. Chem. Lett.* **6** 2944–9
[66] Cheng Y C *et al* 2020 *J. Phys. B: At. Mol. Opt. Phys.*
      54 014001
[67] Rajput J, Kumar H, Bhatt P and Safvan C P 2020 *Sci. Rep.*
      10 1–8
[68] Amini K *et al* 2018 *Struct. Dyn.* **5**
[69] Richardson P J, Eland J H D and Lablanquie P 1986 *Org.
      Mass Spectrom.* **21** 289–94